Carbon 140 (2018) 250–258

Contents lists available at ScienceDirect

Carbon

journal homepage: www.elsevier.com/locate/carbon

Nature of localized phonon modes of tilt grain boundaries in graphene

W.A. Diery [a], Elie A. Moujaes [b], R.W. Nunes [c, *]

[a] *Physics Department, Faculty of Science, King AbdulAziz University, 21589, Jedda, Saudi Arabia*
[b] *Physics Department, Federal University of Rondônia, 76900-900, Porto Velho, Brazil*
[c] *Physics Department, Federal University of Minas Gerais, 31270-901, Belo Horizonte, MG, Brazil*

ARTICLE INFO

Article history:
Received 8 May 2018
Received in revised form
21 August 2018
Accepted 24 August 2018
Available online 29 August 2018

ABSTRACT

In this work, it is reported an investigation of the phonon spectrum of polycrystalline models of graphene, using *ab-initio* calculations of the phonon dispersion and phonon modes of these systems. Four different models of polycrystalline graphene are considered: one where the lattices of adjacent grains have a relative translation between them, with a translational grain boundary connecting the grains, and three models where the lattices of adjacent grains are tilted relative to each other, with tilt grain boundaries connecting adjacent grains. It is found that tilt grain boundaries introduce high-frequency non-dispersive phonon modes in the phonon spectrum of polycrystalline graphene, and that these modes are strongly localized in the core of the grain boundaries, while no such high-frequency localized modes are found in the case of the translational boundary system. By computing phonon group velocities and specific heats of each system in our study, and by analyzing in detail the patterns of atomic displacements of these localized modes, a consistent interpretation is provided for the experimentally observed trends of the lattice thermal conductivity of polycrystalline graphene samples, as a function of the grain-boundary tilt angle.

1. Introduction

Starting with the isolation and identification of single-layer and few-layer graphene - the sp^2-bonded two-dimensional (2D) form of carbon with remarkable electronic and mechanical properties - the Physics of 2D materials has become one of the central topics of research in Condensed Matter and Nanoscale Physics in the 21st century [1–5]. Graphene is a null-gap semiconductor, with a vanishing density of states at the Fermi level. The 2D honeycomb structure of graphene is composed of two sublattices, and its electronic bands are linear and isotropic within ~1eV from the Fermi level. These features imply that charge carriers in this material effectively behave as massless chiral relativistic particles described by Dirac's equation [3,5]. After thirteen years of the graphene breakthrough, scientific interest in graphene is still growing, and the material continues to play a major role in the area of Nanoscale and 2D Physics.

In 2D, properties of materials can be heavily affected by structural irregularities. Graphene edges and point defects, such as vacancies and topological defects, have been thoroughly investigated over the past few years [6,8–11,40]. Of equal importance, from both fundamental science and applications points of view, is the effect of disorder associated with grain boundaries (GB) in polycrystalline systems. These are extended defects characterized by a topological invariant (the Burgers vector) and by the misorientation angle between adjacent grains in a polycrystalline solid [12–14]. They play an important role in controlling the electric and mechanical properties of the polycrystalline system, and generally have different atomic configurations and local atomic densities than the perfect crystal, acting as scattering centers for both electrons and phonons, and as sinks for impurity atoms which tend to segregate to the boundaries [15].

In graphene, GBs are usually produced when the material is grown by deposition methods, such as chemical vapor deposition [16], and commonly occur in graphitic materials, such as graphite [17,18], soot [19,20], fullerenes [21], and carbon nanotubes [22]. In the giant fullerenes considered in Ref. 21, a line of fivefold and sevefold rings, with similar morphology to the GB we consider, closes in itself and spans the diameter of the fullerene. In the case of carbon nanotubes in Ref. 22, extended lines of 5 and 7 rings along the nanotube axis and around the diameter of the tube have been considered theoretically. Besides their usual role in electronic and

---

* Corresponding author.
E-mail address: rwnunes@fisica.ufmg.br (R.W. Nunes).

https://doi.org/10.1016/j.carbon.2018.08.045

thermal transport in polycrystalline samples, scientific interest in graphene grain boundaries has also been motivated by some unusual properties they display, such as bimodal phonon scattering behaviour [23], anomalous strength characteristics [24], and strong chemical sensitivity to adsorbed gas molecules [25], to name a few.

Several atomic-resolution experimental measurements of GB structures in free-standing graphene [26–31], as well as theoretical studies, have been performed on polycrystalline-graphene samples [14,24,32–44]. Among the first experimental results is the scanning tunneling microscopy studies of tilt GBs on graphite surfaces [45]. More recently, it has been shown that grain boundary defects have a dramatic influence on the local electronic properties of graphite [17,18]. On the theoretical side, studies of the impact of GBs on the phonon spectrum and on the scattering of electronic excitations and phonons in graphene have been performed [23,46–48], but these are mostly restricted to molecular dynamics studies, usually based on interatomic potentials.

The focus of the present paper is to investigate the phonon spectrum of polycrystalline models of graphene (poly-Gr), by means of *ab-initio* calculations of the phonon dispersion and of the associated phonon modes in these materials, a task that, to the best of our knowledge, has not been tackled before. We consider four different models of polycrystalline graphene: one where the lattices of adjacent grains have a relative translation between them, with a translational grain boundary connecting the grains, and three other models where the lattices of adjacent grains are tilted relative to each other, with tilt grain boundaries connecting the grains. Each of these systems is characterized by the morphology of the grain boundary between adjacent grains.

We find that tilt grain boundaries introduce non-dispersive high-frequency phonon modes in the phonon spectrum of polycrystalline graphene that are strongly localized in the core of the grain boundaries, while no such localized modes are found in the case of the translational boundary model. By analysing in detail the patterns of atomic displacements of these localized modes, we are able to provide a consistent picture of the experimentally observed trends of the thermal conductivity of polycrystalline graphene samples as a function of the tilt (or misorientation) angle between adjacent grains.

The paper is organized as follows: In section 2, a summary of the four polycrystalline models is provided, with a description of the geometry of the GB in each case, as well as the computational details of the methods used to perform the various electronic and phononic calculations. In section 3, we include results for the phonon spectrum and the phonon density of states (PhDOS) of each system. Section 3 also includes results for properties such as the specific heat capacity at constant volume c_v, and the phonon group velocities for the poly-Gr systems, compared to those of pristine graphene, as well as a discussion of the impact of the GB morphologies on the thermal conductivity of each system in our study, compared to reported experimental results for this property. Summary and conclusions are included in Section 4.

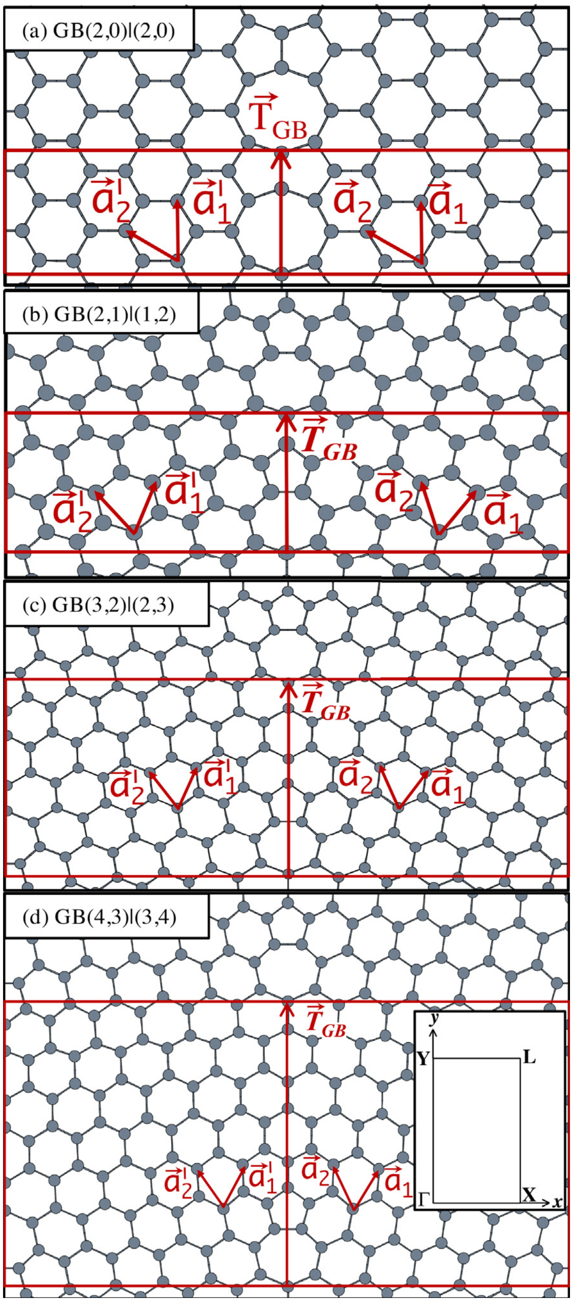

Fig. 1. Geometries of one-dimensional periodic grain boundaries in graphene. Lattice vectors of the left grain ($\vec{a}'_1, \vec{a}'_2$) and of the right grain ($\vec{a}_1, \vec{a}_2$) are shown as red arrows. The vector representing the period of the GB ($\vec{T}_{GB}$) is also shown in red. The GBs are labelled by GB$(n_L, m_L)|(n_R, m_R)$ where $\vec{T}_{GB} = n_L\vec{a}'_1 + m_L\vec{a}'_2 = n_R\vec{a}_1 + m_R\vec{a}_2$. (a) Translational grain boundary: GB(2,0)|(2,0). Tilt grain boundaries: (b) GB(2,1)|(1,2); (c) GB(3,2)|(2,3); and (d) GB(4,3)|(3,4). The red rectangles delineate the supercell employed in the calculations, in each case. The inset in (d) shows the irreducible Brillouin zone for the supercells in (a)–(d), with high-symmetry $\vec{k}$-points indicated. (A colour version of this figure can be viewed online.)

2. Methodology and grain-boundary geometries

The translational grain boundary commonly known as 558 defect [14,31,49–54] is shown in Fig. 1 (a) and the three tilt GB models, based on the experimental images in Ref. 30, are shown in Fig. 1(b)-(d). In Fig. 1, the larger red arrow shows the GB translation vector $\vec{T}_{GB}$ (representing the smallest translation that leaves the GB structure invariant), and the smaller red arrows show the lattice vectors of the grains on the left ($\vec{a}'_1, \vec{a}'_2$) and on the right ($\vec{a}_1, \vec{a}_2$) of the GB. By noting that $\vec{T}_{GB} = n_L\vec{a}'_1 + m_L\vec{a}'_2 = n_R\vec{a}_1 + m_R\vec{a}_2$, we denote the GBs in Fig. 1 as GB $(n_L, m_L)|(n_R, m_R)$ [49]. In this notation, Fig. 1(a) shows the GB(2,0)|(2,0) translational grain boundary (the 558 extended defect), and Fig. 1(b)-(d) show the tilt GBs: GB(2,1)|(1,2), GB(3,2)|(2,3), and GB(4,3)|(3,4), respectively. The inset in Fig. 1(d) shows a schematic representation of the irreducible Brillouin zone (IBZ) for the four supercells in Fig. 1, with the four special $\vec{k}$-points indicated.

The GB(2,0)|(2,0) boundary in Fig. 1(a) is formed by cutting a graphene monolayer along the zigzag direction, and displacing one side of the monolayer by a nearest-neighbor distance with respect to the other side, along an armachir direction. Carbon dimers are then inserted in the seam between the two sides of the layer. Note that the lattices on both sides of the defect have the same orientation, i.e., no tilt is involved in this case.

The model adopted to build the three tilt GB structures relies on the fact that in graphene, these defects consist, in most cases, of periodic structures composed of a regular succession of pentagon-heptagon pairs. In the tilt GB geometries, the tilt angle α depends on the number of lines of hexagonal rings separating the fivefold-sevenfold units along the period of the defect, as described in Ref. 55. We obtain $\alpha = 21.8^\circ$ for the GB(2,1)|(1,2) (with one line of hexagons separating the 5–7 pairs), $\alpha = 13.3^\circ$ for the GB(3,2)|(2,3) (three lines of hexagons), and $\alpha = 9.6^\circ$ for the GB(4,3)|(3,4) (five lines of hexagons), while $\alpha = 0^\circ$ for the GB(2,0)|(2,0).

In the case of tilt GBs, periodicity requires that the supercells in question contain two GBs with opposite Burgers vectors (a GB and the corresponding "anti-GB"), such that the total Burgers vector of the simulation cell vanishes. In the case of the GB(2,0)|(2,0), only one defect line is included in the simulation cell. We consider supercells consisting of 42 atoms for the GB(2,0)|(2,0), 60 atoms for the GB(2,1)|(1,2), 120 atoms for the GB(3,2)|(2,3), and 168 atoms for the GB(4,3)|(3,4). The parameters of the supercells (number of atoms N_a and defect-defect distances d), the GB parameters (period of the defect T_{GB} and tilt angle α) as well as the formation energies (E_f) are included in Table 1. Our results in Table 1 agree well with values previously reported in the literature, as indicated in the table. In particular, the nonmonotonic behaviour of the formation energy as a function of the tilt angle for the GB(2,1)|(1,2), GB(3,2)|(2,3), and GB(4,3)|(3,4) is also obtained in Ref. 38.

Our main goal is to investigate the phonon spectrum of each of the four GB models described above. The first step is to perform electronic structure calculations using the Quantum Espresso (QE) code [56] based on the Density Functional Theory [57]. We use the Rappe-Rabe-Kaxiras-Joannopoulos [58] ultrasoft pseudopotential for the interaction of valence electrons and ion cores, and the generalized gradient approximation, in the Perdew-Burke-Ernzerhof parametrization [59], for the exchange correlation functional.

A tight geometry relaxation was performed until the force on each atom were less than or equal to 1×10^{-5} Ry/a.u., the total energy of the supercells were converged within 0.1 meV/atom, and the pressure on the cell was lower than 0.1 kbar. Monkhorst-Pack [60] k-point sampling of the Brillouin Zone with $12 \times 12 \times 1$, $14 \times 14 \times 1$, $16 \times 16 \times 1$, $18 \times 18 \times 1$ and $30 \times 30 \times 1$ were used for the GB(4,3)|(3,4), GB(3,2)|(2,3), GB(2,1)|(1,2), GB(2,0)|(2,0), and pristine graphene, respectively. From previous work involving one of the authors of this work [49], it is established that 18 k-points along the defect direction is enough to ensure convergence within the above tolerances for the GB(2,0)|(2,0). The samplings for the other defects are excessive, since these tolerances could be met with smaller samplings, in particular in the direction perpendicular to the defect.

A plane wave energy cutoff of 60 Ry and a density cutoff of 600 Ry were found to produce well converged results needed for the subsequent phonon spectrum calculations. In order to stimulate isolated 2D sheets, and since the QE code is based on plane wave basis sets, supercells are taken to be periodic along the graphene plane and surrounded by a 15 Å vacuum, which is large enough to impede interactions of the graphene layer with its periodic images.

The study of the phonon spectra was performed using the PHONOPY code [61] where the full phonon spectrum, phonon eigenvectors, and the corresponding density of states can be calculated using the supercell method, also known as the frozen-phonon approach [62,63]. Our phonon calculations are done using a combination of the QE and PHONOPY codes. Self consistent calculations to converge the structures are performed with QE, and the relaxed structures are then fed to PHONOPY for the phonon calculations.

Since the chosen supercell size influences the convergence of the thermal properties and given the computational limitations in going to higher supercell dimensions, results were obtained using a $1 \times 1 \times 1$ supercell for GB(3,2)|(2,3) and GB(4,3)|(3,4), and a $2 \times 2 \times 1$ for GB(2,0)|(2,0) and GB(2,1)|(1,2) structures. On the other hand for pure graphene with two atoms in the unit cell, an $8 \times 8 \times 1$ supercell was used in PHONOPY to compute the thermal properties.

3. Results and discussions

The electronic properties of the GBs examined in this paper have been already discussed in Refs. [49,55], using the SIESTA code [64]. Since these constitute the initial step for phonon calculations, they have been computed again using the QE code. Results similar to the ones reported in these works were obtained: the electronic structures of the titl GBs [GB(2,1)|(1,2), GB(3,2)|(2,3), GB(4,3)|(3,4)] show a vanishing gap and a Dirac-like nature of electronic excitations, which are common features with pristine graphene. More interestingly is the generation of an anisotropic Dirac cone at the Fermi level, with the Dirac point on a $\overrightarrow{k}$-vector along the GB direction. In the GB(2,0)|(2,0) case, we also obtain the strongly-localized empty electronic states just above the Fermi level that lead to a magnetic instability upon n-type doping, as discussed in Ref. 49.

Converged phonon dispersion relations $\omega(\overrightarrow{q})$, as well as the corresponding PhDOS of pristine graphene with two atoms in the unit cell, along the Γ-M-K-Γ path in the IBZ, computed with a combination of QE and PHONOPY codes are shown in Fig. (2). The phonon dispersion relation of graphene comprises three acoustic (A) branches and three optical (O) branches. The modes are associated with out-of-plane (Z), in-plane longitudinal (L), and in-plane transverse atomic motions [65–67].

As expected, the phonon dispersion relation shows two in-plane acoustic modes with linear dispersions, and a flexural mode with quadratic dispersion, associated with a free translation of the monolayer along the normal direction, that is characteristic of 2D systems. This quadratic mode triggers the intrinsic instability of free-standing 2D materials in the thermodynamic limit [3,68]. Whether graphene should display a flexural mode with quadratic dispersion is a matter of debate in the literature. While Castro Neto *et. al.* [3] argue that such quadratic modes should appear in any 2D system, for it is the free translation of the whole layer in free space (hence with an energy that is quadratic in the momentum) and

Table 1
Number of atoms (N_a), geometric parameters (α, T_{GB} and d), as well as the formation energies per unit length (E_f)of the GBs involved in this work. The two-dimensional crystallographic point group of each structure is indicated in parenthesis. Previously reported values for α, T_{GB}, and E_f, and corresponding references, are indicated for comparison. [1]Ref. 14; [2]Ref. 38; [3]Ref. 40; [4]Ref. 55.

System	N_a	α(degree)	T_{GB}(Å)	d(Å)	E_f(eV/Å)
GB(2,0)|(2,0) (pmm)	42	0.0	4.90 (4.96[3])	22.67	0.48 (0.49[3])
GB(2,1)|(1,2) (pm)	60	21.29 (21.8[2])	6.54 (6.59[2])	12.40	0.33 (0.34[1], 0.32[2], 0.33[4])
GB(3,2)|(2,3) (pm)	120	13.30 (13.2[2])	10.90 (10.65[2])	14.70	0.41 (0.36[2], 0.42[4])
GB(4,3)|(3,4) (pm)	168	9.60 (10.9[2])	15.20 (14.83[2])	14.74	0.39 (0.30[2], 0.40[4])

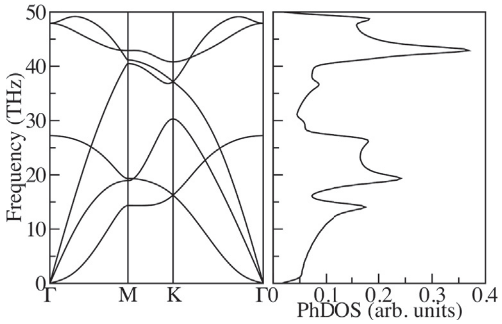

Fig. 2. Phonon spectrum and density of states of pristine graphene with two atoms in the unit cell along the Γ-M-K-Γ path in the Brillouin zone. The quadratic flexural mode near the Γ point causes a non-zero DOS at zero frequency.

Mariani and von Oppen [69] argue that the quadratic dispersion is a result of rotation and reflexion symmetries, Adamyan *et. al.* [70] claim that inclusion of non-linear terms render the dispersion of the flexural mode linear, with a velocity of sound that differs from that of the regular in-plane acoustic modes.

The linear crossings of the ZA/ZO and the LA/LO modes at the K-point arise due to the D_{6h} point-group symmetry of graphene. The finite PhDOS at zero frequency, that can be observed in Fig. 2, is due to the van Hove singularity of the flexural mode with quadratic dispersion. It is also instructive to note that according to group theoretical analysis [71], the lattice vibrational modes at the Γ point can be decomposed as $2A''_2 + 2E'$, where the A''_2 modes are infrared active and the E' are Raman active.

For a comparison of the phonon dispersions of the poly-Gr systems at hand with that of pristine graphene, we show in Fig. 3 the phonon dispersions of the four poly-Gr models. In each case, given the supercell sizes involved, the number of phonon modes is quite high and there is substantial band folding due to the smallness of the corresponding IBZs. The band plots however clearly show a very distinct feature of the phonon dispersion relations of the tilt GBs: the appearance of high-frequency flat phonon branches (shown as red lines) in Fig. 3(b)-(d), respectively for the GB(2,1)|(1,2), the GB(3,2)|(2,3), and the GB(4,3)|(3,4), at frequencies above the highest phonon frequency ($\omega \sim$49.2 THz) we obtain in the pristine-graphene dispersion in Fig. 2. Of importance also is the fact that such high-frequency flat modes are absent in the phonon dispersion of the translational boundary GB(2,0)|(2,0) in Fig. 3(a).

Further comparison between the phonon spectra of pristine graphene and the poly-Gr systems is best pursued by comparing the respective PhDOS. In Fig. 4, the red curves show the PhDOS for each poly-Gr supercell, with the phonon DOS of pristine graphene shown in black for comparison. A few general observations can be drawn from Fig. 4. In all four cases, in the frequency interval between 0 and 5 THz, where the pristine graphene phonon DOS is quite smooth, a DOS peak appears in the polycrystalline models at ω = 3.4 THz for the GB(2,1)|(1,2), $\omega \sim$ 4.5 THz for the GB(3,2)|(2,3), $\omega \sim$4.8 THz for the GB(2,1)|(1,2), and $\omega \sim$ 5.0 THz for the GB(2,0)|(0,2). Note that the frequency of this peak tends to the value of 5 THz as the tilt angle α decreases. At frequencies higher than 5 THz, the phonon spectra of the poly-Gr systems are similar to that of the pristine system, except for the splitting of the peaks in the intervals $16 \leq \omega \leq$ 30 THz and $40 \leq \omega \leq$50 THz, an effect of degeneracy lifting due to the lower symmetry in the polycrystalline models. Finally, as discussed in the previous paragraph, the tilt GB models display rather flat phonon modes at frequencies above 50 THz, as shown in Fig. 4(b)-(d).

In order to investigate in more detail the nature of the localized modes in the tilt GBs, in Fig. 5 we show the amplitude of the atomic displacements of the eigenmodes of the lowest of the flat phonon branches of the tilt GBs, on the Γ and Y special $\vec{k}$-points of the IBZ shown in the inset in Fig. 1(d). The higher-frequency ($\sim$48 THz) phonon branch of the GB(2,0)|(2,0) is also shown for comparison. We note that in the case of the tilt GBs, we have two GBs in the supercell, hence the displacements of the atoms of the two boundaries are independent degrees of freedom.

Fig. 5(a) shows the amplitude of atomic displacements for the ω = 48 THz modes of the GB(2,0)|(2,0) [the highest-frequency branch in the phonon spectrum of Fig. 3(a)] at the Γ and Y points of the IBZ shown in Fig. 1(d). Atomic displacements are shown as a function of the perpendicular distance of each atom (or group of atoms) to the line going through the geometric center of the defect core, which in the GB(2,0)|(2,0) is defined by the common side of the two pentagons. Atoms to the right (left) of the GB are ascribed a positive (negative) distance such that the symmetry of the mode with respect to the GB line is displayed. The non-localized nature of this GB(2,0)|(2,0) phonon branch is clearly displayed in Fig. 5, with sizeable displacements of all atoms in the supercell for the two modes depicted in the figure.

In the case of the tilt GBs, the geometric center of the defect (with respect to which distances are measured) is the median of the pentagon-heptagon pair, going through the nadir of the hexagon and the apex of the pentagon. By zooming in on the interval of frequencies above 50 THz in the GB(2,1)|(1,2) phonon dispersion in Fig. 3(b), it can be observed that each one of the two high-frequency flat modes consists of a pair of nearly degenerate non-dispersive phonon branches, one pair at $\sim$50.1 THz with a splitting of $\sim$0.1 THz between them, and another at $\sim$50.6 THz, also with a $\sim$0.1 THz splitting. The reason for the small splittings is that the supercells for the tilt GBs have an inversion center that is slightly broken, numerically, because we did not enforce the inversion center in the calculation. Similar considerations apply for the set of three flat modes of the GB(3,2)|(2,3) and the GB(4,3)|(3,4) in Fig. 3(c) and (d).

Fig. 5(b) displays the amplitude of atomic displacements for the $\omega \sim$50.1 THz modes of the GB(2,1)|(1,2), at the Γ and Y points of the IBZ. This is the lowest of the two flat phonon branches in the phonon dispersion for this defect in Fig. 3(b). Given the degeneracy, the two modes can be chosen as non-inversion-symmetric combinations of the inversion-symmetric modes. The non symmetric modes are inversion images of each other, localized on either one of the two GBs in the cell. The localized nature of this mode is clear in the figure, with high amplitudes of atomic motion for atoms near the defect, and a fast decay of the amplitudes as we move into the bulk region of the supercell.

Fig. 5(c) and (d) show the lowest-frequency flat phonon branches for the GB(3,2)|(2,3) ($\omega \sim$51.6 THz) and the GB(4,3)|(3,4) ($\omega \sim$52.2 THz), respectively. Again, strong localization of these non-dispersive phonon branches on the GB region is clearly displayed in Fig. 5(c) and (d), with high values of atomic displacements for atoms near the GB and a fast decay as we move into the bulk region of the supercells. The apparent ressurgance of the modes starting at a distance of $\sim$12 Å from the center of the GB is due to the fact that in this region the neighborhood of the other GB in the supercell is reached.

Let us discuss now the impact of such localized modes on phononic transport in polycrystalline graphene. Phonon transport is determined, among other factors, by the group velocity v_g of the phonon modes. In Fig. 6(a) and (b) we show the profile of group-velocity values for pristine graphene and for the GB(2,1)|(1,2) boundary, respectively. The figures clearly show a strong overall tendency of lower group velocities in the polycrystalline model, with a much higher concentration of modes with $v_g \leq$ 8 km/s than in the pristine case. Moreover, we observe a marked increase in the

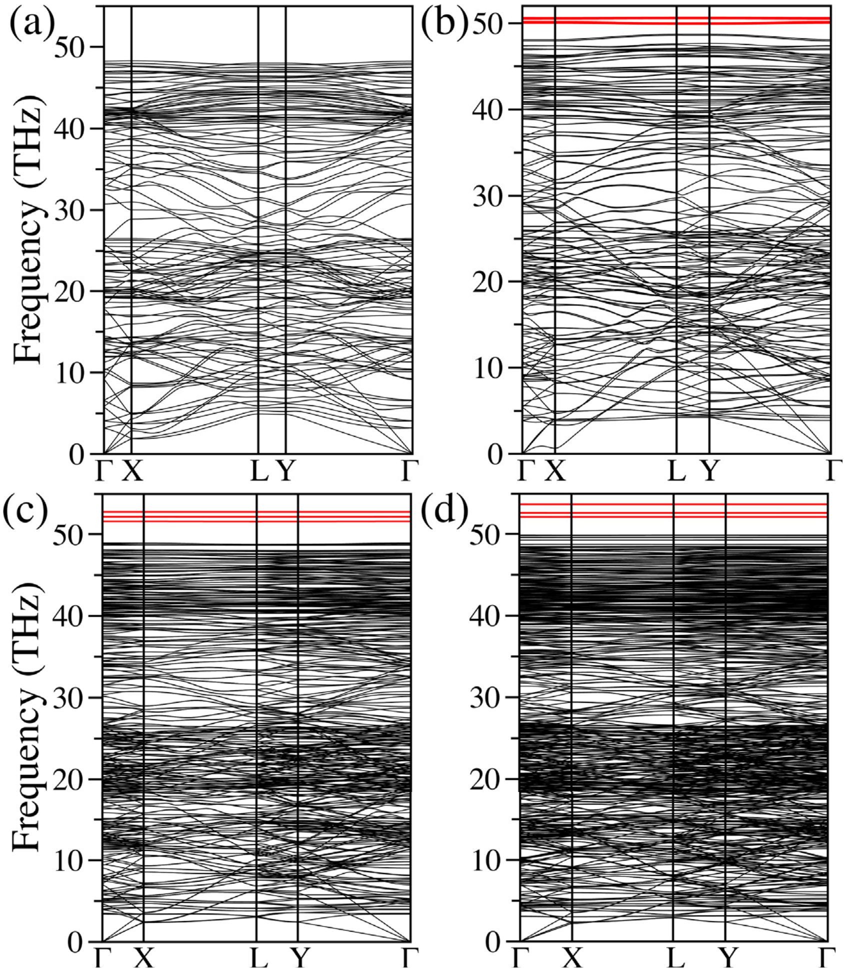

Fig. 3. Phonon dispersion relations for polycrystalline models of graphene. (a) GB(2,0)|(2,0); (b) GB(2,1)|(1,2); (c) GB(3,2)|(2,3); (d) GB(4,3)|(3,4). High-frequency flat modes appear as red horizontal lines. (A colour version of this figure can be viewed online.)

number of modes with null group velocity, signaling the emergence of non-dispersive modes in the polycrystalline model, not only in the high-frequency range of the aforementioned localized modes, but also over the entire interval of phonon frequencies in Fig. 6(b). To be more quantitative, the red bars in the two panels in Fig. 6 show the average group velocity for the two systems. The average velocity for pristine graphene (7.25 km/s) is about twice as large as the average value for the GB(2,1)|(1,2) boundary (3.57 km/s). Furthermore, for the GB(2,1)|(1,2) 74.8% of the modes we computed have $v_g \le 5.0$ km/s and 11.4% have $v_g \le 0.5$ km/s, while for pristine graphene the corresponding fractions are 36.4% and 1.2%. The patterns of group velocities for the other tilt boundaries in our study (not shown in Fig. 6) are very similar, with an increase in the number of null-velocity modes and an overall downward shift in the distribution of group velocity values.

Another parameter that impacts the transport of phonons and electrons in materials is the scattering of these excitations by localized phonon modes, because localized modes tend to locally enhance the electron-phonon coupling and the anharmonic effects that lead to strong phonon-phonon scattering. Hence, the emergence of localized modes in the polycrystalline models in our study is bound to reduce the phonon lifetimes and, along with the reduction of group velocities, this feature should also strongly impact transport properties.

Indeed, previous experimental and theoretical studies have shown a reduction in the lattice thermal conductivity κ in polycrystalline graphene compared to pristine graphene, and that the values of κ correlate with the GB tilt angle α, with a tendency of increasing values of κ as α decreases [23]. In order to correlate these trends with our results, we recall that the lattice thermal conductivity tensor, as implemented in the PHONO3PY code [72], is given by

$$\kappa_{\alpha\beta} = \frac{1}{NV_0}\sum_{\overrightarrow{q},s} c_v(\overrightarrow{q},s)v_\alpha(\overrightarrow{q},s)v_\beta(\overrightarrow{q},s)\tau(\overrightarrow{q},s) \quad (1)$$

where $c_v(\overrightarrow{q},s)$, $v_{\alpha(\beta)}(\overrightarrow{q},s)$, and $\tau(\overrightarrow{q},s)$ are, respectively, the specific heat, the group velocity, and the phonon lifetime for the $(\overrightarrow{q},s)$ phonon mode. In the above equation, the sum is over all wavevectors q and their branch indices s, and N, V_0 and $\tau(\overrightarrow{q},s)$ represent, respectively, the total number of sampling points, the volume of the unit cell and the phonon lifetime for the mode $(\overrightarrow{q},s)$, and $\alpha(\beta) = \{x, y\}$, since the structures are two dimensional.

We have already discussed the reduction of group velocities in the poly-Gr models. Fig. 7 shows the specific heat (integrated over the Brillouin zone) computed for pristine graphene and for each poly-Gr system in our study, for six different temperatures. At room temperature, we obtain $c_v \sim 0.71$J/(K.g) for pristine graphene, which is in agreement with previously reported values in the literature [73]. For all temperatures, c_v values for the poly-Gr models differ from those of graphene by ~10% or less. At room

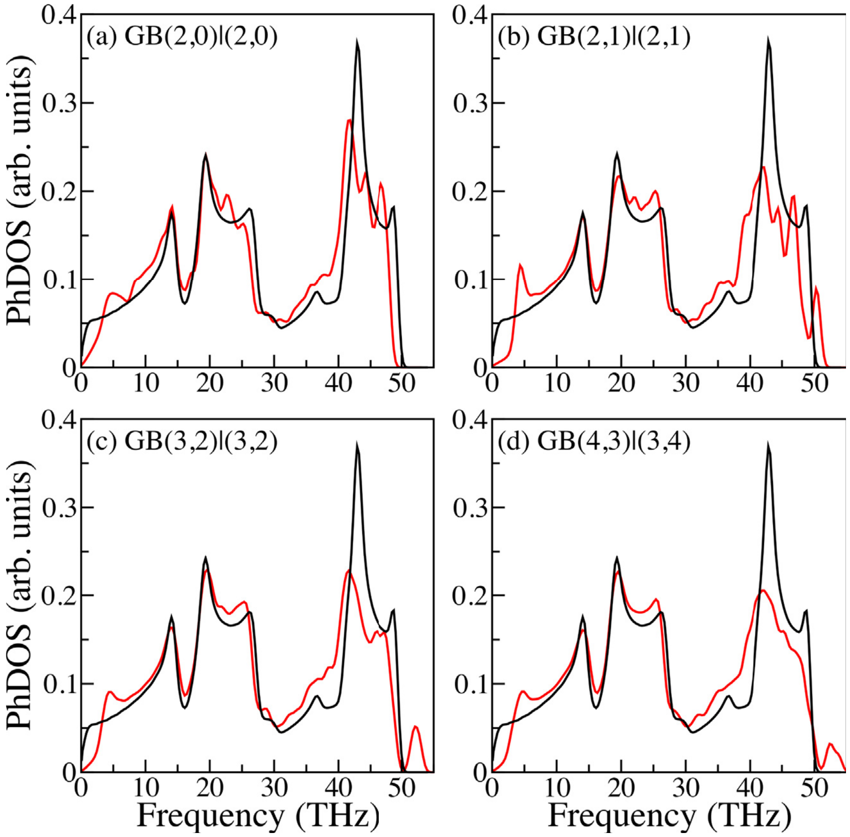

Fig. 4. Red curves show the phonon density of states (PhDOS) for polycrystalline models of graphene. (a)GB(2,0)|(2,0); (b) GB(2,1)|(1,2); (c) GB(3,2)|(2,3); (d) GB(4,3)|(3,4). Black curves show PhDOS for pristine graphene, for comparison. (A colour version of this figure can be viewed online.)

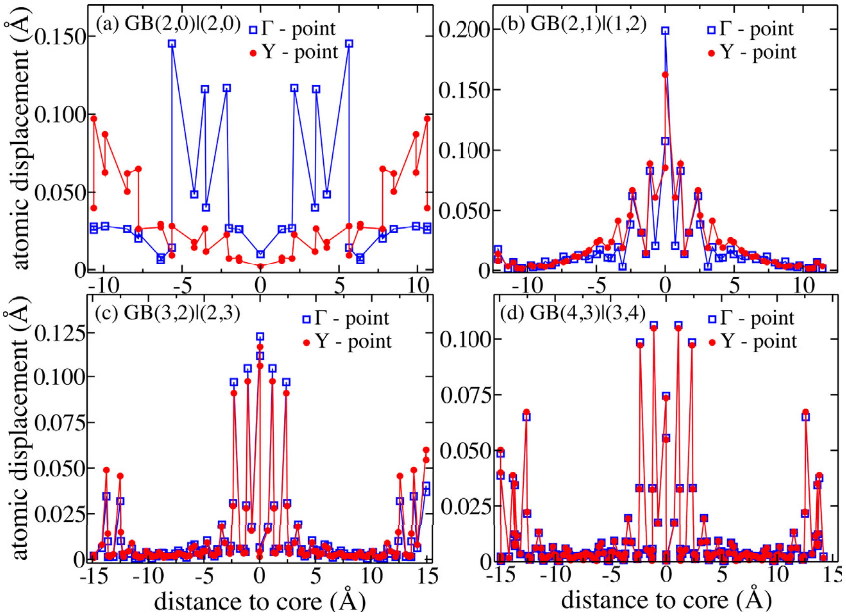

Fig. 5. Mass-normalized amplitudes of atomic displacements corresponding to the high-frequency flat modes (red curves in Fig. 3) of polycrystalline graphene. Displacements are plotted, for the four high-symmetry points in the IBZ [inset in Fig. 1(d)], as a function of the distance to the center of the grain boundary. Localized nature of the flat modes for the tilt GBs is clearly displayed. (a) GB(2,0)|(2,0); (b) GB(2,1)|(1,2); (c) GB(3,2)|(2,3); GB(4,3)|(3,4). (A colour version of this figure can be viewed online.)

temperature, c_v results for the poly-Gr systems are only ~3–4% larger than the pristine graphene value, and should have a minor impact in the values of κ for these systems.

Another factor in the above equation for κ is the phonon lifetime, that cannot be obtained from a ground-state calculation as in the present study. Nevertheless, a closer inspection of the pattern of

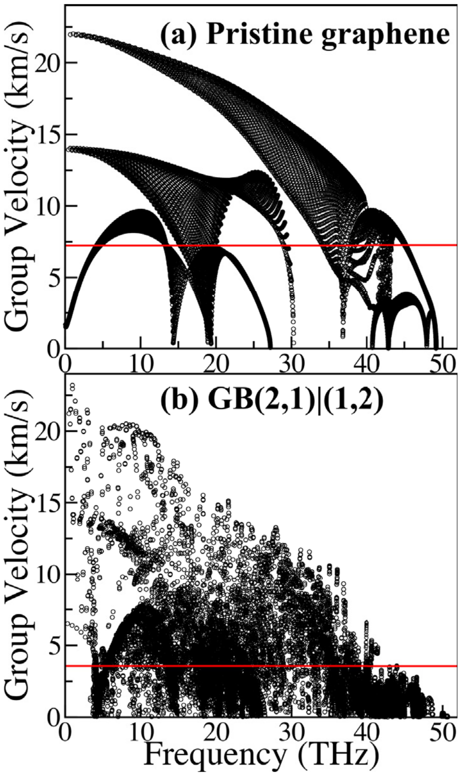

Fig. 6. Distribution of phonon group velocities for (a) pristine graphene and (b) the GB(2,1)|GB(1,2) model for polycrystalline graphene. Red horizontal bars indicate the value of the average group velocity for each distribution. (A colour version of this figure can be viewed online.)

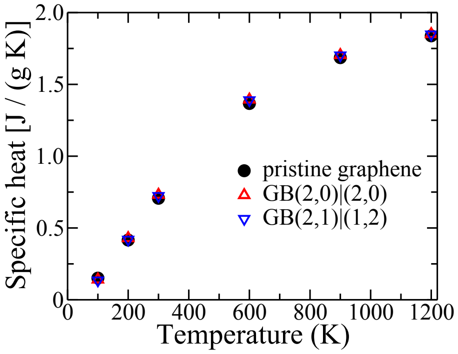

Fig. 7. Specific heat capacity at constant volume c_v, as a function of temperature, for pristine graphene and for the polycrystalline models, in units of J/(K.g). (A colour version of this figure can be viewed online.)

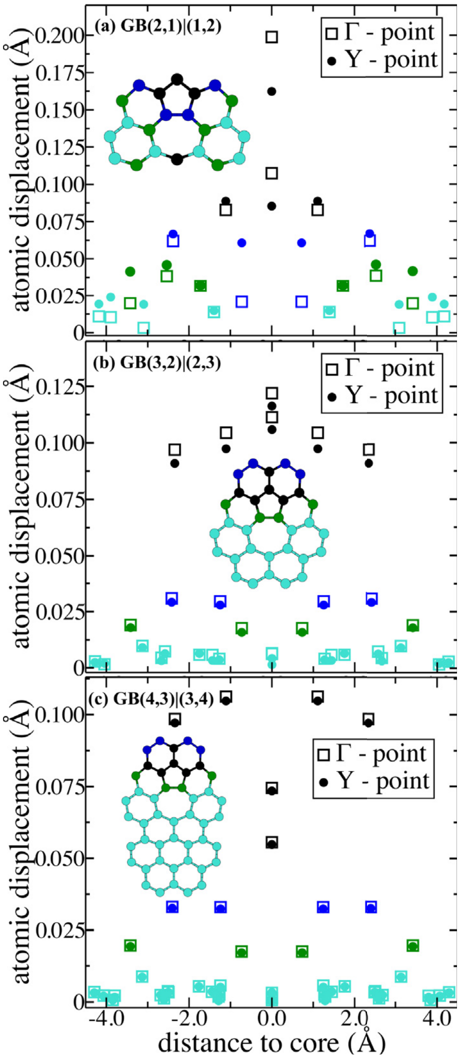

Fig. 8. Pattern of atomic displacements, in the neighborhood of the grain-boundary core, for the high-frequency flat phonon modes in polycrystalline graphene. (a) GB(2,1)|(1,2); (b) GB(3,2)|(2,3); and GB(4,3)|(3,4). In each panel, the inset show atoms at and near the grain-boundary core, color-coded according to the range of atomic displacements indicated in the figure: black symbols show atoms with high-values of the displacement amplitude; blue symbols show atoms with medium-to-high amplitudes; green symbols show atoms with medium-to-low displacements; and turquoise-blue symbols show atoms with low values of atomic displacements. (A colour version of this figure can be viewed online.)

amplitudes of the atomic displacements of the localized modes, in the neighborhood of the grain boundaries, provides information that allows us to form a qualitative picture of the aforementioned experimental trends of κ as a function of α.

For this, in Fig. 8 we plot the amplitude of atomic displacements in the GB core and its immediate neighborhood, for the lowest of the flat modes of the tilt GBs in Fig. 3, at the Γ and Y points of the IBZ. In each case, we show the amplitude for atoms at the core and its neighborhood as a function of the distance to the geometric center of the core. Displacement values are divided in four intervals, with the following color coding: black squares and circles, show high amplitude atoms, blue symbols show medium-to-high amplitude atoms, green symbols show medium-to-low displacement atoms, while low displacement atoms are shown as turquoise symbols. In each case, the inset shows the atoms at the core of the defect and its immediate neighborhood. Atoms in the inset are color coded according to the symbols in the plot, to show the corresponding displacement amplitudes.

A first general observation is that magnitudes of atomic displacements in these flat modes decrease with increasing α, and we should expect a decrease in phonon scattering by the GBs as α increases, in line with the aforementioned experimental trends. Furthermore, we note that in these tilt GBs large atomic displacements are concentrated on the region of the vertex of the pentagon that is opposite to the heptagon. This is consistent with the fact that the pentagon is the compression side of the edge dislocation (an isolated pentagon-heptagon pair is an edge dislocation in graphene), with smaller bond lengths and hence with stiffer bonds, as found in Ref. 74. The bottom of the heptagon is the tension side of the dislocation, and we observe smaller displacements in this region.

Note that in the tilt GBs with larger angles [GB(3,2)|(2,3) and GB(4,3)|(3,4)] this low-displacement region extends to the lines of hexagons between the dislocations along the core of the defect. The pristine-like morphology of these portions of the core imply that these are low-phonon-scattering regions. Hence, within the structural model of tilt grain boundaries we adopt, the low-scattering regions in the core of the defect increase with increasing α, and we should expect that phonon-scattering by the GB core should decrease with increasing α. These observations are fully consistent with the experimental findings observed in Ref. 23.

4. Conclusion and discussion

In this work, we report an investigation of the phonon spectrum of polycrystalline models of graphene, by means of *ab-initio* calculations of their phonon dispersion and of the associated phonon modes. We consider four different models of polycrystalline graphene. One with lattices of adjacent grains translated relative to each other, connected by a translational grain boundary that shows fused topological defects (fivefold and eightfold rings). The other three models have the lattices of adjacent grains misoriented relative to each other, connected by symmetric tilt grain boundaries that show lines of prisitine-like hexagons separating the fivefod and sevenfold rings along the core.

We find that tilt grain boundaries introduce high-frequency non-dispersive phonon modes in the phonon spectrum of polycrystalline graphene, and that these modes are strongly localized on the core of the grain boundaries. No such high-frequency localized modes are found in the case of the translational-boundary system, where no tilt occurs between the grains. We compute the phonon group velocities and specific heats (at six different temperatures) of each system in our study, and find that while specific heats of the polycrystalline systems are quite similar to that of graphene, the distribution of group velocities is very different, with an overall tendency of lower group-velocity values and an increase in the number of modes with null group velocities in the polycrystalline systems, when compared to pristine graphene.

By analysing in detail the patterns of atomic displacements of the high-frequency localized modes in the polycrystalline systems, we propose a consistent interpretation for the experimentally observed trends of increasing values of the lattice thermal conductivity of polycrystalline graphene samples as the tilt angle decreases. In our analysis, we propose that the increase in the pristine-like, low-scattering regions, in the core of the grain boundaries, as the tilt angle decreases, explains the experimentally observed trends for the thermal conductivity of the polycrystalline samples.

Our present analysis is limited to the symmetric titl grain-boundary models we address, and the only model we consider in the present work that has fused topological defects does not display the localized modes that we find in the symmetric tilt boundaries. We are currently undertaking calculations of non-symmetric tilt grain boundaries that present fused topological defects in their core, with no pristine-like hexagons separating the topological defects, in order to find out to which extent we can generalize the correlations between the occurrence of localized phonon modes (and their respective patterns of atomic displacements) and the grain-boundary morphology and tilt angle in polycrystalline graphene.

Acknowledgments

The simulations in this work were performed at King Abdulaziz University's High Performance Computing Center (Aziz HPCC) (http://hpc.kau.edu.sa). R. W. Nunes acknowledges support from Brazilian agencies CNPq, FAPEMIG (Edital-Universal grants: APQ-02290-14 and APQ-03312-17), and INCT de Nanomateriais de Carbono.

Appendix A. Supplementary data

Supplementary data related to this article can be found at https://doi.org/10.1016/j.carbon.2018.08.045.

References

[1] A.K. Geim, K.S. Novoselov, The rise of graphene, Nat. Mater. 6 (2007) 183.
[2] M.I. Katsnelson, Graphene:carbon in two dimensions, Mater. Today 10 (2007) 20.
[3] A.H. Castro Neto, F. Guinea, N.M.R. Peres, K.S. Novoselov, A.K. Geim, The electronic properties of graphene, Rev. Mod. Phys. 81 (2009) 109.
[4] K. Nakada, M. Fujita, G. Dresselhaus, M.S. Dresselhaus, Edge state in graphene nanoribbons: nanometer size effect and edge shape dependence, Phys. Rev. B 54 (1996) 17954.
[5] P.R. Wallace, The band theory of graphite, Phys. Rev. 71 (1947) 622.
[6] L.R. Radovic, B. Bockrath, On the chemical nature of graphene edges:origin of stability and potential for magnetism in carbon materials, J. Am. Chem. Soc. 127 (2005), 59175927.
[8] I. Zsoldos, Effects of topological defects on graphene geometry and stability, Nanotechnol. Sci. App. 3 (2010) 101–106.
[9] J. Da Silva-Araújo, H. Chacham, R.W. Nunes, Gap opening in topological-defect lattices in graphene, Phys. Rev. B 81 (2010) 193405.
[10] P.T. Araujo, M. Terrones, M.S. Dresselhaus, Defects and impurities in graphene-like materials, Mater. Today 15 (2012) 98–109.
[11] Y.N. Xu, D. Zhan, L. Liu, H. Suo, Z.H. Ni, T.T. Nguyen, et al., Thermal dynamics of graphene investigated by polarized Raman spectroscopy, ACS Nano 3 (2009) 569–574.
[12] J.P. Hirth, J. Lothe, Theory of Dislocations. Institute of Physics. Oslo University, McGraw-Hill Book Company, New York, 1972.
[13] D.R. Nelson, Defects and Geometry in Condensed Matter Physics, Cambridge Univ. Press, Cambridge, 2002.
[14] O.V. Yazyev, S.G. Louie, Topological defects in graphene: dislocations and grain boundaries, Phys. Rev. B 81 (2010) 195420.
[15] S.L. Sass, Grain Boundaries, McGraw-Hill Education, AccessScience, 2014.
[16] Y. Zhang, L. Zhang, C. Zhou, Review of chemical vapor deposition of graphene and related applications, Acc. Chem. Res. 46 (2013) 23292339.
[17] J. Červenka, C.F.J. Flipse, The role of defects on the electronic structure of a graphite surface, Phys.: Conf. Ser. 61 (2007) 190.
[18] J. Červenka, M. Katsnelson, C.F.J. Flipse, Room-temperature ferromagnetism in graphite driven by two-dimensio al networks of point defects, Nat. Phys. 5 (2009) 840–844.
[19] S. Iijima, T. Wakabayashi, Y.J. Achiba, Structures of carbon soot prepared by laser ablation, Phys. Chem. 100 (1996) 5839–5843.
[20] J.-O. Müller, D.S. Su, R.E. Jentoft, T.J. Krhner, F.C. Jentoft, R. Schlgl, Morphology-controlled reactivity of carbonaceous materials towards oxidation, Catal. Today 102 (2005) 259–265.
[21] M. Terrones, G. Terrones, H. Terrones, Structure, chirality and formation of giant icosahedral fullerenes and spherical graphitic onions, Struct. Chem. 13 (2002) 373–384.
[22] J.C. Charlier, Defects in carbon nanotubes, Acc. Chem. Res. 35 (2002) 1063.
[23] P. Yasaei, A. Fathizadeh, R. Hantehzadeh, A.K. Majee, A. El-Ghandour, D. Estrada, et al., Bimodal phonon scattering in graphene grain boundaries, Nano Lett. 15 (2015), 45324540.
[24] R. Grantab, V.B. Shenoy, R.S. Ruoff, Anomalous strength characteristics of tilt grain boundaries in graphene, Science 330 (2010) 946.
[25] P. Yasaei, B. Kumar, R. Hantehzadeh, M. Kayyalha, A. Baskin, N. Repnin, et al., Chemical sensing with switchable transport channels in graphene grain boundaries, Nat. Commun. 5 (2014) 4911.
[26] P.Y. Huang, C.S. Ruiz-Vargas, V.M. van der Zande, W.S. Whitney, M.P. Levendorf, J.W. Kevek, et al., Grains and grain boundaries in single-layer graphene atomic patchwork quilts, Nature 469 (2011) 389–392.
[27] K. Kim, Z. Lee, W. Regan, C. Kisielowski, M. Crommie, A. Zettl, Grain boundary mapping in polycrystalline graphene, ACS Nano 5 (2011) 2142.
[28] H.I. Rasool, C. Ophus, Z. Zhang, M.F. Crommie, B.I. Yakobson, A. Zettl, Conserved atomic bonding sequences and strain organization of graphene grain boundaries, Nano Lett. 14 (2015) 7057–7063.
[29] C. Ophus, A. Shekhawat, H. Rasool, A. Zettl, Large-scale experimental and theoretical study of graphene grain boundary structures, Phys. Rev. B 92 (2015) 205402.
[30] P. Simonis, C. Goffaux, P.A. Thiry, L.P. Biro, Ph Lambin, V. Meunier, STM study of a grain boundary in graphite, Surf. Sci. 511 (2002) 319–322.
[31] J. Lahiri, Y. Lin, P. Bozkurt, Oleynik II, M. Batzill, An extended defect in graphene as a metallic wire, Nat. Nanotech. 5 (2010) 326–329.
[32] J.B. Oliveira, I.S. Santos de Oliveira, J.E. Padilha, R.H. Miwa, Tunable magnetism

and spin-polarized electronic transport in graphene mediated by molecular functionalization of extended defects, Phys. Rev. B 97 (2018) 045107.

[33] W.H. Brito, R. Kagimura, R.H. Miwa, B and N doping in graphene ruled by grain boundary defects, Phys. Rev. B 85 (2012), 035404.

[34] S. Malola, H. Häkkinen, P. Koskinen, Structural, chemical, and dynamical trends in graphene grain boundaries, Phys. Rev. B 81 (2010) 165447.

[35] E. Cockayne, G.M. Rutter, N.P. Guisinger, J.N. Crain, P.N. First, J.A. Stroscio. Grain boundary loops in graphene. Phys. Rev. B (83) 195425.

[36] J.M. Carlsson, L.M. Ghiringhelli, A. Fasolino, Theory and hierarchical calculations of the structure and energetics of [0001] tilt grain boundaries in graphene, Phys. Rev. B 84 (2011) 165423.

[37] L. Yi, Z. Yin, Y. Zhang, T. Chang, A theoretical evaluation of the temperature and strain-rate dependent fracture strength of tilt grain boundaries in graphene, Carbon 51 (2013) 373.

[38] J. Zhang, J. Zhao, J. Lu, Intrinsic strength and failure behaviors of graphene grain boundaries, ACS Nano 6 (2012) 2704.

[39] Q.Q. Dai, Y.F. Zhu, Q. Jiang, Electronic and magnetic properties of armchair graphene nanoribbons with 558 grain boundary, Phys. Chem. Chem. Phys. 16 (2014) 10607.

[40] J. Sun, N. Lin, Z. Li, H. Ren, C. Tanga, X. Zhao, Electronic and transport properties of graphene with grain boundaries, RSC Adv. 6 (2016) 1090.

[41] P. Vancsó, G.I. Márk, P. Lambin, A. Mayer, C. Hwang, L.P. Biró, Effect of the disorder in graphene grain boundaries: a wave packet dynamics study, Appl. Surf. Sci. 291 (2014) 58–63.

[42] Z. Song, V.I. Artyukhov, B.I. Yakobson, Z. Xu, Pseudo HallPetch strength reduction in polycrystalline graphene, Nano Lett. 13 (2013) 1829–1833.

[43] F. Hao, D. Fang, Mechanical deformation and fracture mode of polycrystalline graphene: atomistic simulations, Phys. Lett. 376 (2012) 1942.

[44] J. Kotakoski, J.C. Meyer, Mechanical properties of polycrystalline graphene based on a realistic atomistic model, Phys. Rev. B 85 (2012) 195447.

[45] T.R. Albrecht, H.A. Mizes, J. Nogami, S-i Park, C.F. Quate, Observation of tilt boundaries in graphite by scanning tunneling microscopy and associated multiple tip effects, Appl. Phys. Lett. 52 (1988) 362.

[46] C. Kimmer, S. Aubrey, A. Skye, P.K. Schelling, Scattering of phonons from a high-energy grain boundary in silicon: dependence on angle of incidence, Phys. Rev. B 75 (2007) 144105.

[47] P. Schelling, S.R. Phillpot, P. Keblinski, Kapitza conductance and phonon scattering at grain boundaries by simulation, J. Appl. Phys. 95 (2004) 6082–6091.

[48] H.-S. Kim, S.D. Kang, Y. Tang, R. Hanus, G.J. Snyder, Dislocation strain as the mechanism of phonon scattering at grain boundaries, Mater. Horiz. 3 (2016) 234–240.

[49] S.S. Alexandre, A.D. Lúcio, A.H. Castro Neto, R.W. Nunes, Correlated magnetic states in extended one-dimensional defects in graphene, Nano Lett. 12 (2012), 509-5102.

[50] S.S. Alexandre, R.W. Nunes, Magnetic states of linear defects in graphene monolayers: effects of strain and interaction, Phys. Rev. B 96 (2017), 075445.

[51] L.C. Gomes, S.S. Alexandre, H. Chacham, R.W. Nunes, Stability of edges and extended defects on boron nitride and graphene monolayers: the role of chemical environment, J. Phys. Chem. C 117 (2013) 11770–11779.

[52] A.J.M. Nascimento, R.W. Nunes, Lubrication of Stone-Wales transformations in graphene by hydrogen and hydroxyl functional groups, Nanotechnology 24 (2013) 435707.

[53] J. da Silva-Araújo, A.J.M. Nascimento, H. Chacham, R.W. Nunes, Non-hexagonal-ring defects and structures induced by healing and strain in graphene and functionalized graphene, Nanotechnology 24 (2013) 035708.

[54] A. Hashimoto, K. Suenaga, A. Gloter, K. Urita, S. Iijima, Direct evidence for atomic defects in graphene layers, Nature (London) 430 (2004) 870.

[55] J. da Silva Araújo, R.W. Nunes, Complex evolution of the electronic structure from polycrystalline to monocrystalline graphene: generation of a new Dirac point, Phys. Rev. B 81 (2010) 073408.

[56] P. Giannozzi, S. Baroni, N. Bonini, N. Calandra, R. Car, C. Cavazzoni, et al., QUANTUM ESPRESSO: a modular and open-source software project for quantum simulations of materials, J. Phys. Condens. Matter 21 (2009) 395502.

[57] G. Kresse, Furthmüller, Efficient iterative schemes for ab initio total-energy calculations using a plane-wave basis set, J. Phys. Rev. B 54 (1996) 11169.

[58] A.M. Rappe, K.M. Rabe, E. Kaxiras, J.D. Joannopoulos, Optimized pseudopotentials, Phys. Rev. B 41 (1990) 1227.

[59] J. Perdew, K. Burke, M. Ernzerhof, Generalized gradient approximation made simple, Phys. Rev. Lett. 77 (1996) 3865.

[60] H.J. Monkhorst, J.D. Pack, Special points for Brillouin-zone integrations, Phys. Rev. B 13 (1976) 5188.

[61] A. Togo, F. Oba, I. Tanaka, First-principles calculations of the ferroelastic transition between rutile-type and CaCl$_2$-type SiO$_2$ at high pressures, Phys. Rev. B 78 (2008) 134106.

[62] A. van de Walle, M. Asta, G. Ceder, The alloy theoretic automated toolkit: a user guide, J. Calphad. 26 (2002) 539553.

[63] K. Parliński, Z.Q. Li, Y. Kawazoe, First-Principles determination of the soft mode in cubic ZrO$_2$, Phys. Rev. Lett. 78 (1997), 40634066.

[64] J.M. Soler, E. Artacho, J.D. Gale, A. Garcia, J. Junquera, P. Ordejon, D. Sanchez-Portal, The SIESTA method for ab initio order-N materials simulation, J. Phys. Condens. Matter 14 (2002) 2745.

[65] R. Saito, G. Dresselhaus, M. Dresselhaus, Physical Properties of Carbon Nanotubes, Imperial College Press, London, 1998.

[66] O. Dubay, G. Kresse, Accurate density functional calculations for the phonon dispersion relations of graphite layer and carbon nanotubes, Phys. Rev. B 67 (2003), 035401.

[67] L. Wirtz, A. Rubio, The phonon dispersion of graphite revisited, Solid State Commun. 131 (2004) 141–152.

[68] N.D. Mermin, H. Wagner, Absence of ferromagnetism or antiferromagnetism in one- or two-dimensional isotropic heisenberg models, Phys. Rev. Lett. 17 (1966) 1133.

[69] Mariani, F. Von Oppen, Flexural phonons in free-standing graphene, Phys. Rev. Lett. 100 (2008), 076801.

[70] V. Adamyan, V. Zavalniuk, Lattice thermal conductivity of graphene with conventionally isotopic defects, J. Phys. Condens. Matter 24 (2012) 415401.

[71] X. Zhang, X.F. Qiao, W. Shi, J.B. Wu, D.S. Jiang, P.H. Tan, Phonon and Raman scattering of two-dimensional transition metal dichalcogenides from monolayer, multilayer to bulk material, Chem. Soc. Rev. 44 (2015) 2757–2785.

[72] A. Togo, L. Chaput, I. Tanaka, Distributions of phonon lifetimes in Brillouin zones, Phys. Rev. B 91 (2015), 094306.

[73] S. Mann, P. Rani, R. Kumar, G.S. Dubeyc, V.K. Jindal, Thermodynamic properties of pure and doped (B, N) graphene, RSC Adv. 6 (2016) 12158–12168.

[74] A. Mackiewicz, T. Bark, B. Cao, J.A. Delaire, D. Riehl, W.L. Ling, S. Foillard, E. Doris, Fullerene-functionalized carbon nanotubes as improved optical limiting devices, Carbon 49 (2011) 3998–4003.